Practice article

Air flow rate and pressure control approach for the air supply subsystems in PEMFCs

Meng Li [a,b], Hai Yin [a], Tianwei Ding [c], Jing Zhao [d], Jinwu Gao [a,b,*], Hong Chen [b,e]

[a] State Key Laboratory of Automotive Simulation and Control, Jilin University, Changchun 130022, China
[b] Department of Control Science and Engineering, Jilin University, Changchun 130022, China
[c] Research and Development Institute, China FAW Group Company, Changchun 130013, China
[d] School of Mechanical Engineering and Automation, Northeastern University, Shenyang 110819, China
[e] Department of Control Science and Engineering, Tongji University, Shanghai 200092, China

ARTICLE INFO

ABSTRACT

Simultaneous control of the air flow rate and the cathode pressure plays an essential role in enhancing the performance and prolonging the service life of a polymer electrolyte membrane fuel cell (PEMFC). However, this is challenging to implement in practice due to the high complexity and coupled dynamics of the air supply subsystem in the PEMFC. This work, based on a simplified control-oriented model, puts forward a disturbance-observer-based multi-output feedback control strategy to address the issue of synergistically controlling the air flow rate and cathode pressure. The disturbances (Including humidity, temperature, water vapor, etc.) are estimated through an extended state observer (ESO). The final control law, which takes the disturbances observation into account, is designed through feedback linearization technique. A complex, high-order, nonlinear model is used as the high-fidelity plant in the validation process, and a series of simulations are implemented under different operational conditions. The outcomes show that the proposed control strategy offers a rapid dynamic response, precise steady-state tracking performance, and strong robustness against disturbances and unmodeled dynamics.

1. Introduction

A polymer electrolyte membrane fuel cell (PEMFC) is an electrochemical device that converts the chemical energy of hydrogen and oxygen into electrical energy and has been widely applied in diverse fields [1]. In particular, for automotive applications, the PEMFC is regarded as the most promising substitute for conventional engines due to its low noise, zero pollution, high efficiency, and high power density [2,3].

For a high-power PEMFC used in automobiles, the air supply subsystem transient behavior plays a vital role in achieving the desired power and prolonging the service life of the PEMFC [4]. Among the numerous characteristics, the air flow rate into the cathode and cathode pressure are the two most critical variables [5]. A low air flow rate may lead to oxygen starvation, which may damage the polymer electrolyte membrane (PEM) owing to the inadequate electrochemical reactions. In contrast, a high air flow rate may increase the parasitic power to nearly 30% of the total power of the PEMFC [6–8]. Furthermore, a change in the

air flow rate affects the cathode pressure. A high cathode pressure can increase the amount of air reaching the catalytic layer through the diffusion layer due to the large differential pressure, thereby enhancing the catalytic rate. However, the instantaneous differential pressure between the cathode and anode may impact the PEM, leading to irreversible damage to the PEMFC [9,10].

So far, a lot of research has been done on system modeling and control strategy development for the air supply subsystem. Several control-oriented models of the air supply subsystem have been proposed. Pukrushpan et al. [11] developed a system-level model, which laid the groundwork for the subsequent research. In this model, the dynamic characteristics of the compressor, supply manifold, humidifier, cathode, and return manifold were mathematically described. Suh et al. [12] developed a fourth-order model to facilitate the design of the controller, without considering the dynamics of the humidifier and return manifold. Talj et al. [13] replaced the oxygen pressure and the nitrogen pressure with the cathode pressure, further deriving a third-order model. Based on a commercially available 1 kW fuel cell stack, in which the air is controlled by a fan, Ramospaja et al. [14] derived a simplified model for low-power PEMFCs. However, all of the above models are only applicable to single-input single-output systems, which cannot perform multi-objective control tasks.

* Corresponding author at: State Key Laboratory of Automotive Simulation and Control, Jilin University, Changchun 130022, China.
E-mail address: gaojw@jlu.edu.cn (J. Gao).

With the control-oriented models, many control strategies have been implemented to regulate the oxygen excess ratio in the air supply subsystems. For example, a linear quadratic regulator (LQR) controller was developed based on the linearization model obtained by Taylor expansion [11]. Due to the complexity of the air supply subsystem, linear models are often limited in representing the nonlinear transients. Chen et al. [15] applied the feedback linearization control method to track the variable optimal oxygen excess ratio, where satisfying experimental results were obtained when the model matched the system dynamics well. Sliding mode controls (SMCs) were developed to improve the regulation of the oxygen excess ratio during a transient subsequent to an abrupt change in load current [16–19]. Although SMC can address the uncertainties and nonlinear characteristics, control variable chatter is usually generated near the equilibrium point under a high feedback gain, which is detrimental to the system. Ma et al. [20] analyzed the net power output of the PEMFC under different oxygen excess ratio and then regulated the oxygen excess ratio using a nonlinear triple-step method. Hu et al. [21] applied a disturbance-observer-based nonlinear triple-step method for oxygen excess ratio control. The simulation results show that the control strategy performs a good effect on the desired oxygen excess ratio tracking and disturbance rejection. Gruber et al. [22] and Ouan et al. [23] applied different nonlinear model predictive control (NMPC)-based solutions to regulate the oxygen excess ratio for the air supply subsystem. Although NMPC can solve the issue of nonlinear system dynamics and control variable constraints, the excessive optimization time poses a challenge in ensuring the system's real-time performance. Notably, the abovementioned methods focused only on the control of the oxygen excess ratio without considering cathode pressure control, which may lead to a considerable differential pressure between the cathode and anode. Therefore, ensuring synergistic control of the cathode pressure and the air flow rate (or oxygen excess ratio) is imperative.

Suitable air flow rate and cathode pressure are usually achieved by using a compressor to control the air flow rate into the cathode and a throttle to control the air flow rate out of the cathode. However, mutual coupling exists between the air flow rate into the cathode and the cathode pressure. Up to now, only limited research about coordinated control of the air flow rate into the cathode and the cathode pressure has been conducted. Ahmed et al. [5] investigated the gain schedule LQR control to regulate the air flow rate and cathode pressure, while this strategy did not cover all PEMFC operating conditions and thus had limited applicability in practice. Fonseca et al. [24] and Danzer et al. [7] used different differential-flatness-control-based strategies to track the oxygen excess ratio and cathode pressure. However, this approach requires that the model can reflect the dynamic characteristics of the plant with high accuracy, which brings challenges to the modeling.

Motivated by the abovementioned studies, this work aims to realize the synergistic control of the air flow rate and the cathode pressure and compensate for the unmodeled dynamics, thereby reducing the modeling efforts, which represents a significant advantage over the previous works. To simplify the controller design and reduce the effort required in the modeling, a control-oriented fourth-order model is proposed. Moreover, a control strategy combining an extended state observer (ESO) and feedback linearization technique is developed to overcome disturbances and unmodeled dynamics of the air supply subsystem. In detail, the ESO is designed to observe disturbances and unmodeled dynamics, the estimated values of which are used in the control law design through feedback linearization technique to ensure the stability and closed-loop performance of the air supply subsystem. The main innovation of this work is to provide an effective control strategy to simultaneously regulate the air flow rate and the cathode pressure with low dependence on the model accuracy.

The remainder of this paper is organized as follows: a control-oriented fourth-order model is developed in Section 2. Then, this paper compares the differences between the model and plant and further analyzes the rationality and usability of the model. In Section 3, a disturbance-observer-based feedback linearization control strategy is designed. The simulation results are presented in Section 4. Finally, the conclusion is drawn in Section 5.

2. System modeling and analysis

A typical structure of a PEMFC is shown in Fig. 1. Oxygen from the cathode of the air supply subsystem reacts electrochemically with hydrogen from the anode of the hydrogen supply subsystem to power the load, and the water and heat management subsystems provide the proper humidity and temperature environment for the electrochemical reaction. Fig. 2 presents the structure of the air supply subsystem. The operating mechanism of the air supply subsystem is as follows: Through a filter, air enters the compressor, which regulates the flow rate. The air then enters the cathode, in which the electrochemical reaction occurs, through an intercooler and a humidifier. The air passes through a water–air separation device. Finally, the water vapor enters the exhaust water tank, and dry air is discharged through the throttle. In this process, the compressor supply voltage and throttle opening command are used as the manipulation variables to synergistically control the air flow into the cathode and cathode pressure. In this work, the high-fidelity model of the air supply subsystem in [11] is utilized as the original plant. The exhaust port of the original plant is uncontrolled and considered to be a single-input single-output system. Thus, we add a throttle as a new actuator in the original plant to work with the compressor to regulate the air flow into the cathode and cathode pressure. In addition, experimental data of a real compressor in our laboratory (The specific test conditions and steps are introduced in the section of "Modeling of the centrifugal air compressor") are used to replace the original compressor data. In this manner, a new plant (unless otherwise specified, "new plant" is denoted by "plant") has been established, which will be used for simulation to verify the control strategy.

Notably, the dynamic characteristics of the air supply subsystem in the plant are influenced by many factors, such as the air humidity, operating temperature, electrochemical reaction rate inside the cathode, water migration, and water vapor dynamics, which render the system model complex and the controller design challenging. To achieve synergistic control of the air flow into the cathode and cathode pressure, a simplified model is developed in this section to capture the plant's main features. The air supply subsystem is simplified into the following four parts:

(1). Centrifugal air compressor: to regulate the air flow rate;
(2). Air supply manifold: to connect the compressor and fuel cell stack;
(3). Cathode: to provide suitable conditions for an electrochemical reaction;
(4). Throttle: to control the flow rate of the exhaust air from the fuel cell stack.

2.1. Modeling of the air supply subsystem

2.1.1. Modeling of the centrifugal air compressor

The centrifugal air compressor is suitable for use with the PEMFC due to its high air flow and relatively low compression rate. This device plays a crucial role in the air supply subsystem because the air flow rate can be changed by adjusting the speed
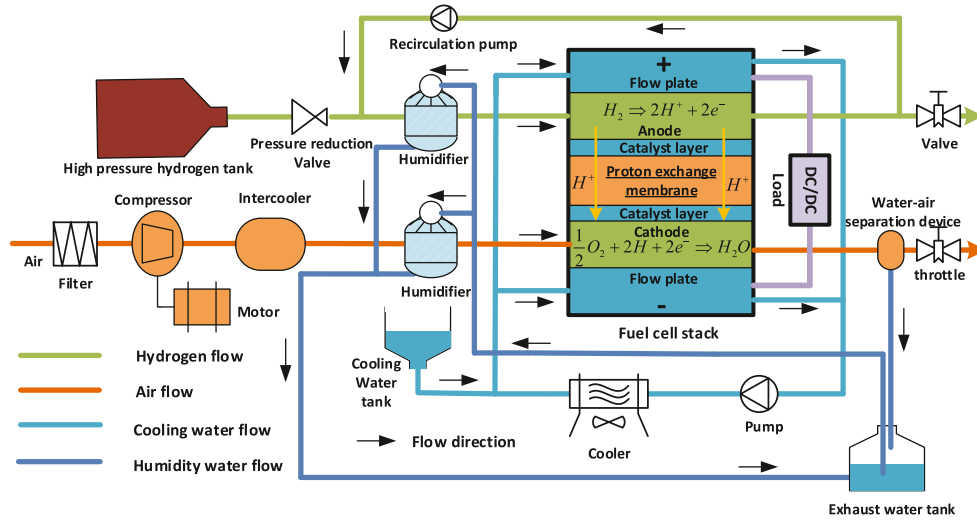
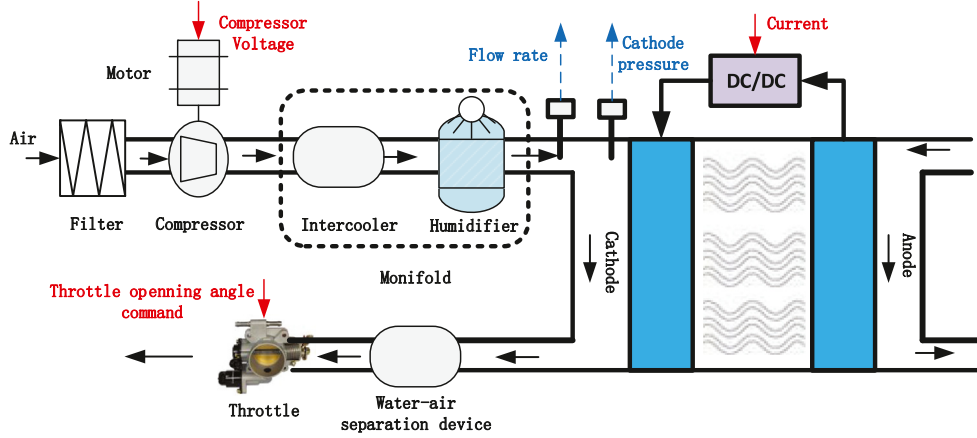**Fig. 1.** Complete PEMFC system structure schematic [25].

Fig. 2. Air supply subsystem structure schematic.

of the compressor. The compressor dynamics are modeled using the lump rotational parameter principle:

$$\frac{d\omega_{cp}}{dt} = \frac{1}{J_{cp}}\left(\tau_{cm} - \tau_{cp}\right), \tag{1a}$$

$$\tau_{cm} = \eta_{cm}\frac{k_t}{R_{cm}}\left(v_{cm} - k_v\omega_{cp}\right), \tag{1b}$$

$$\tau_{cp} = \frac{C_p}{\omega_{cp}}\frac{T_{atm}}{\eta_{cp}}\left[\left(\frac{p_{sm}}{p_{atm}}\right)^{\frac{\gamma-1}{\gamma}} - 1\right]W_{cp}, \tag{1c}$$

where J_{cp} denotes the inertia of the compressor; ω_{cp} is the angular velocity of rotation, whose conversion relationship with the compressor speed, N_{cp}, is $\omega_{cp} = 2\pi N_{cp}/60$; τ_{cm} represents the compressor torque input; τ_{cp} represents the torque required to drive the compressor; v_{cm} is the compressor voltage; p_{sm} denotes the air supply manifold pressure; p_{atm} represents the atmospheric pressure; T_{atm} represents the atmospheric temperature; C_p denotes the specific heat capacity; γ denotes the ratio of specific heat; η_{cp} represents the maximum compression efficiency; η_{cm}, k_t, R_{cm}, and k_v are the mechanical constants of the compressor. Flow rate W_{cp} is determined by compressor speed N_{cp} and pressure ratio $\frac{p_{sm}}{p_{atm}}$. We have tested the compressor with a maximum speed of 100,000 RPM to obtain flow rate, pressure and temperature data.
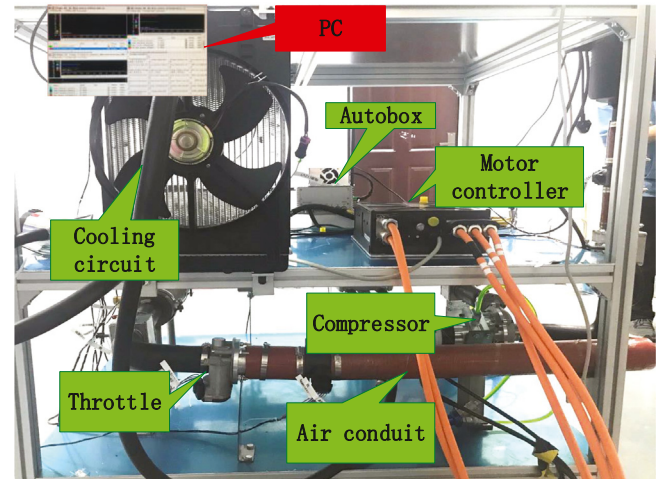

Fig. 3. Compressor test bench.

The compressor test bench, as shown in Fig. 3, mainly consists of a compressor, a motor controller, a cooling circuit, an air conduit, an Autobox, a throttle, and a personal computer (PC). The working process of the entire system is as follows: The PC

Table 1
Polynomial fitting result.

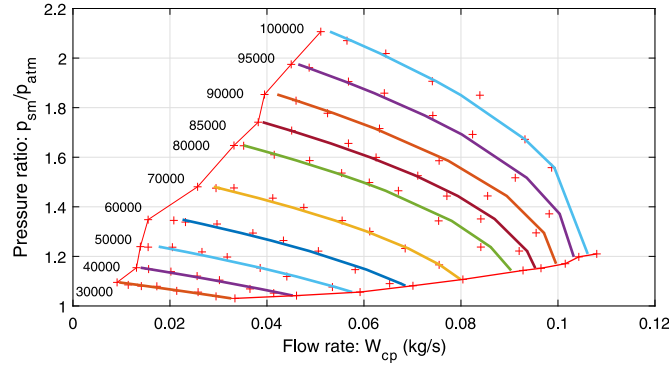| Index	Order		
	First-Order	Second-Order	Third-Order
RMSE	0.0049	0.0021	0.0019
SSE	0.0022	0.0003	0.0004
CC	0.9817	0.9969	0.9971
RS	0.9637	0.9971	0.9947

Fig. 4. Comparison of the experimental data and fitting results, where the fitting coefficients are as follows: $p_1 = -9.229308165951 * 10^{-6}$, $p_2 = 6.629425656160 * 10^{-6}$, $p_3 = 0.3057744134726$, $p_4 = 7.24454764418886 * 10^{-11}$, $p_5 = -0.5009635776762$, $p_6 = -7.89209536275 * 10^{-11}$, $p_7 = 4.28968869210773 * 10^{-6}$, and $p_8 = 0.1928170417443$.

sends control commands to the motor controller through the Autobox to regulate the compressor speed and throttle opening angle. The sensor signals (air flow, air temperature, air pressure, coolant flow, and throttle opening angle position), as well as the compressor status signals (speed, motor temperature, voltage, and current), are transmitted to the PC via the Autobox. Since the centrifugal air compressor considered in this paper usually functions at more than 30,000 RPM, the flow rate is measured starting from 30,000 RPM. Note that the pressure ratio is adjusted by changing the throttle opening angle. The specific test steps are as follows:

(Step 1): Set the compressor speed to 30,000 RPM and the throttle valve opening to 85 degrees (maximum throttle opening). Note that the throttle opening must be set from large to small to avoid the compressor surge.

(Step 2): Gradually reduce the throttle valve opening, and record the current flow rate and pressure until the surge zone approaches.

(Step 3): Reopen the throttle opening to 85 degrees, and repeat the previous steps. When the speed reaches 80,000 RPM, measure the sets of data at 5000 RPM intervals until 100,000 RPM (Note that the operation sequence must not be changed).

A total of 89 sets of experimental data are recorded. Polynomial fitting is applied to fit the data into nonlinear relations. Four evaluation indicators (RMSE: root mean square error, SSE: sum of squared errors, CC: correlation coefficient, and RS: R-squared) are used to analyze and compare the effects between the first-, second-, and third-order polynomials. As shown in Table 1, the first-order polynomial exhibits a larger deviation, while the second- and third-order polynomials exhibit a high accuracy. The second-order polynomials are less complex than the third-order polynomials. Therefore, the continuous differentiable form of W_{cp}

can be derived through a second-order polynomial fitting:

$$
\begin{aligned}
W_{cp}\left(N_{cp}, \frac{p_{sm}}{p_{atm}}\right) &= p_1 N_{cp} + p_2 N_{cp}\frac{p_{sm}}{p_{atm}} + p_3\frac{p_{sm}}{p_{atm}} + p_4 N_{cp}^2 \\
&+ p_5\left(\frac{p_{sm}}{p_{atm}}\right)^2 \\
&+ p_6 N_{cp}^2\frac{p_{sm}}{p_{atm}} + p_7 N_{cp}\left(\frac{p_{sm}}{p_{atm}}\right)^2 + p_8,
\end{aligned}
\tag{2}
$$

where $p_i, i \in \{1, \ldots, 8\}$ are fitting coefficients. As shown in Fig. 4, the red scatter points are the experimental data, and the solid lines represent the fitting curves. Almost all the data lie on the fitting curves.

2.1.2. Modeling of the air supply manifold

The air supply manifold connects the compressor and cathode of the PEMFC. The dynamics of air pressure p_{sm} inside the air supply manifold can be represented by Eq. (3) according to the ideal gas law:

$$
\frac{dp_{sm}}{dt} = \frac{T_{cp}R_a}{V_{sm}}\left(W_{cp} - W_{sm}\right),
\tag{3}
$$

where R_a represents the gas constant of air, V_{sm} represents the volume of the manifold, and T_{cp} denotes the temperature of the air leaving the compressor, calculated using Eq. (4) presented in [26]:

$$
T_{cp} = T_{atm} + \frac{T_{atm}}{\eta_{cp}}\left[\left(\frac{p_{sm}}{p_{atm}}\right)^{\frac{\gamma-1}{\gamma}} - 1\right],
\tag{4}
$$

and W_{sm} represents the flow rate out of the air supply manifold, which is equal to the flow rate into the cathode, approximated by the linear form of the nozzle flow equation:

$$
W_{sm} = k_{sm}\left(p_{sm} - p_{ca}\right),
\tag{5}
$$

where k_{sm} is the flow constant and p_{ca} is the cathode pressure.

2.1.3. Modeling of the cathode

The dynamic of the cathode describes the changes in the air pressure. This dynamic can be defined using the ideal gas equation and electrochemical equation:

$$
\frac{dp_{ca}}{dt} = \frac{R_a T_{st}}{V_{ca}}\left(W_{sm} - W_{ca,out}\right) - \frac{R_{O_2} T_{st}}{V_{ca}}W_{O_2,react},
\tag{6}
$$

where V_{ca} and R_{O_2} denote the cathode volume and oxygen gas constant, respectively, and T_{st} represents the operating temperature in the cathode. The oxygen consumption rate $W_{O_2,react}$ is calculated as a function of the load current I_{st}:

$$
W_{O_2,react} = \frac{n_{cell}M_{O_2}}{4F}I_{st},
\tag{7}
$$

where n_{cell} is the number of cells in series in the PEMFC, M_{O_2} is the oxygen molar mass, and F is the Faraday constant.

The nonlinear nozzle equation is used to compute the outlet air flow rate $W_{ca,out}$, as indicated in [27]:

$$
W_{ca,out} = \sin^2\left(\frac{\theta\pi}{180}\right)\frac{C_{D,tr}A_{T,tr}p_{ca}}{\sqrt{\bar{R}T_{st}}} \times (\gamma)^{\frac{1}{2}}\left(\frac{2}{\gamma+1}\right)^{\frac{\gamma+1}{2(\gamma-1)}},
\tag{8}
$$

where $C_{D,tr}$ denotes the throttle discharge coefficient, $A_{T,tr}$ is the maximum throttle opening area, $\bar{R}$ represents the universal gas constant, and θ represents the throttle opening angle regulating the flow rate out of the cathode.

Table 2
Parameters a_t.

$a_1 = \frac{\eta_{cm} k_t k_v}{J_{cp} R_{cm}}$	$a_2 = \frac{C_p T_{atm}}{J_{cp} \eta_{cp}}$
$a_3 = p_{atm}$	$a_4 = \frac{\gamma - 1}{\gamma}$
$a_5 = \frac{\eta_{cm} k_t}{J_{cp} R_{cm}}$	$a_6 = \frac{R_a T_{atm}}{V_{sm}}$
$a_7 = \frac{1}{\eta_{cp}}$	$a_8 = k_{sm}$
$a_9 = \frac{R_a T_{st} k_{sm}}{V_{ca}}$	$a_{10} = \frac{\tilde{R} T_{st} n_{cell}}{4 V_{ca} F}$
$a_{11} = \frac{R_a T_{st}}{V_{ca}} \frac{C_{D,tr} A_{T,tr}}{\sqrt{R T_{st}}} \left(\frac{1}{\gamma}\right)^{\frac{1}{2}} \left(\frac{2}{\gamma + 1}\right)^{\frac{\gamma + 1}{2(\gamma - 1)}}$	$a_{12} = T_{tr}$

2.1.4. Modeling of the throttle

The exhaust gas first passes through the "water-air separation" device; then, the water enters the "exhaust water tank" for humidification, and the dry gas is discharged to the atmospheric environment through the throttle. Therefore, the throttle can adjust the outlet flow and subsequently the cathode pressure by varying the opening angle. In our model, the throttle is assumed to be closed-loop controlled, and thus, its dynamic behavior can be approximated as a first-order system:

$$\dot{\theta} = \frac{1}{T_{tr}} \left(-\theta + \theta^*\right), \tag{9}$$

where T_{tr} represents the response time constant of the throttle, and θ^* denotes the throttle opening angle command.

2.2. State-space representation

We define the state vector as

$$x = \begin{bmatrix} x_1 & x_2 & x_3 & x_4 \end{bmatrix}^T = \begin{bmatrix} \omega_{cp} & p_{sm} & p_{ca} & \theta \end{bmatrix}^T. \tag{10}$$

By combining Eqs. (1) and (9), a nonlinear space–state system can be obtained as

$$\dot{x}_1 = -a_1 x_1 - \frac{a_2}{x_1} \left(\left(\frac{x_2}{a_3}\right)^{a_4} - 1\right) \times h(x_1, x_2) + a_5 u_1, \tag{11a}$$

$$\dot{x}_2 = a_6 \left[1 + a_7 \left(\left(\frac{x_2}{a_3}\right)^{a_4} - 1\right)\right] \times [h(x_1, x_2) - a_8 (x_2 - x_3)], \tag{11b}$$

$$\dot{x}_3 = a_9 x_2 - a_{10} \xi - \left(a_{11} \sin^2\left(\frac{x_4 \pi}{180}\right) + a_9\right) x_3, \tag{11c}$$

$$\dot{x}_4 = \frac{1}{a_{12}} \left(-x_4 + u_2\right), \tag{11d}$$

where $\begin{bmatrix} u_1 & u_2 \end{bmatrix}^T = \begin{bmatrix} v_{cm} & \theta^* \end{bmatrix}^T$ denote the control inputs, $\xi = I_{st}$ is generally considered to be a measurable disturbance, and $h(x_1, x_2) = W_{cp}$. The parameters $a_t, \iota \in \{1, \ldots, 12\}$ are given in Table 2.

By expressing $y_1 = W_{sm}$ (W_{sm} is defined in Eq. (5)) and $y_2 = p_{ca}$, the output equations of the controlled outputs can be presented as

$$y_1 = a_8(x_2 - x_3), \tag{12a}$$

$$y_2 = x_3. \tag{12b}$$

2.3. Model validation

All the values of the physical parameters of the model are given in Table A.1. The dynamic characteristics of the model and plant are compared under different load currents, compressor voltages, and throttle opening angle commands, which are set as step-changed signals, as shown in Fig. 5. In Fig. 6, the solid red line and blue dotted line represent the simulation results of

plant and model, respectively. The maximum flow rate error is 0.01968 kg/s, and the relative error is 44.20% at 14.5 s. In addition, the average relative error is 24.75%. Similarly, the maximum cathode pressure error between the plant and model is 27,100 Pa, and the relative error is 22.58% at 14.5 s. In addition, the average relative error is 8% over 30 s.

The above simulation results indicate that large steady-state deviations exist between the control-oriented model and plant. However, the model's dynamic characteristics are generally consistent with those of the plant. The leading cause of error is the lack of consideration of the dynamic characteristics of water vapor inside the cathode in the model. Other factors, such as the humidity and temperature, are characterized by a low rate of change compared to the air dynamics. Therefore, the model mismatch can be observed and compensated for by using a high-performance controller. In practice, accurately modeling the water dynamic characteristics of the air supply systems as well as the humidity and temperature is difficult. To reduce the modeling effort, this paper compensates for the model mismatch and disturbances by designing an observer and developing a controller to implement tracking control, as described in the next section.

3. Controller design

As mentioned in Section 2, the simulation results exhibit a notable steady deviation between the model and plant, which is expected to adversely affect the system's stability and tracking performance. Therefore, in this section, we propose an ESO, which provides satisfactory level of accuracy and fast convergence for estimating the disturbances and unmodeled dynamics. Then the estimated values are used in the multi-output feedback control law design through the feedback linearization.

3.1. Disturbance observation

By implementing the time derivative of y_1 and y_2 in Eq. (12), two affine formulations of the model can be obtained as follows:

$$\ddot{y}_1 = F_1\left(x, \dot{x}, \xi, \dot{\xi}\right) + \begin{bmatrix} \psi_{11}(x) & \psi_{12}(x) \end{bmatrix} \begin{bmatrix} u_1 & u_2 \end{bmatrix}^T, \tag{13a}$$

$$\ddot{y}_2 = F_2\left(x, \dot{x}, \xi, \dot{\xi}\right) + \begin{bmatrix} \psi_{21}(x) & \psi_{22}(x) \end{bmatrix} \begin{bmatrix} u_1 & u_2 \end{bmatrix}^T, \tag{13b}$$

where the concrete expressions of $F_i\left(x, \dot{x}, \xi, \dot{\xi}\right), i \in \{1, 2\}$ and $\psi_{j,i}(x), j \in \{1, 2\}$, are

$$F_1 = a_8 a_6 \left[a_7 a_4 \left(\frac{x_2}{a_3}\right)^{a_4 - 1} \frac{1}{a_3}\right] \dot{x}_2[(x_1, x_2) - a_8 (x_2 - x_3)] \tag{14a}$$

$$+ a_8 a_6 \left[1 + a_7 \left(\left(\frac{x_2}{a_3}\right)^{a_4} - 1\right)\right]$$

$$\times \left[\frac{\partial h(x_1, x_2)}{\partial x_1} \left(-a_1 x_1 - \frac{a_2}{x_1} \left(\left(\frac{x_2}{a_3}\right)^{a_4} - 1\right)\right) h(x_1, x_2)\right.$$

$$+ \frac{\partial h(x_1, x_2)}{\partial x_2} \dot{x}_2 - a_8 \dot{x}_2 + a_8 \dot{x}_3 \bigg]$$

$$- a_8 \left(a_9 \dot{x}_2 - a_{10} \dot{\xi} - a_{11} \sin^2\left(\frac{x_4 \pi}{180}\right) \dot{x}_3 - a_9 \dot{x}_3\right)$$

$$+ a_8 x_3 a_{11} 2 \sin\left(\frac{x_4 \pi}{180}\right) \cos\left(\frac{x_4 \pi}{180}\right) \frac{\pi}{180} \left(-\frac{1}{a_{12}} x_4\right),$$

$$\psi_{11} = \frac{\partial h(x_1, x_2)}{\partial x_1} a_8 a_6 \left[1 + a_7 \left(\left(\frac{x_2}{a_3}\right)^{a_4} - 1\right)\right] a_5, \tag{14b}$$

$$\psi_{12} = -a_8 \left(-x_3 a_{11} 2 \sin\left(\frac{x_4 \pi}{180}\right) \cos\left(\frac{x_4 \pi}{180}\right) \frac{\pi}{180} \frac{1}{a_{12}}\right), \tag{14c}$$
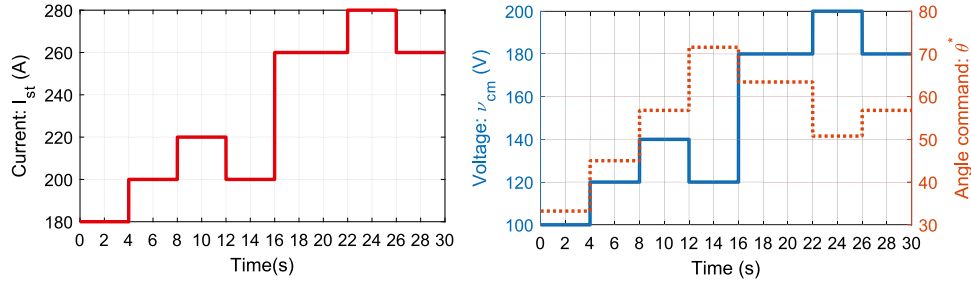
Fig. 5. Step changes in the load current, compressor voltage, and angle command for model comparison.
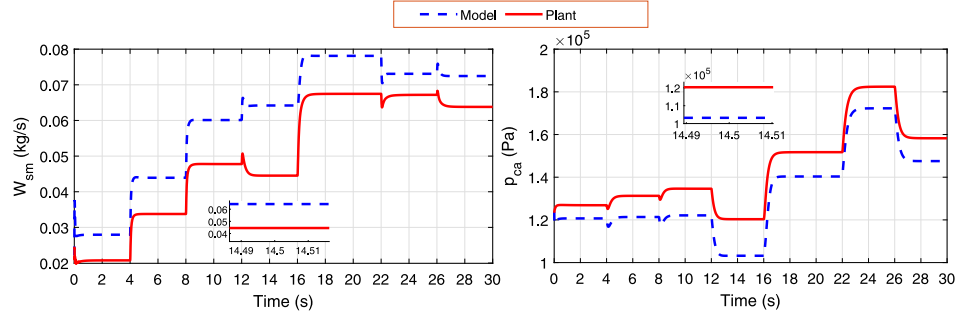

Fig. 6. Model comparison for the flow rate W_{sm} and cathode pressure p_{ca}.

$$F_2 = a_9\dot{x}_2 - a_{10}\dot{\xi} - a_{11}\sin^2\left(\frac{x_4\pi}{180}\right)\dot{x}_3 - a_9\dot{x}_3 \tag{14d}$$

$$- x_3 a_{11} 2 \sin\left(\frac{x_4\pi}{180}\right)\cos\left(\frac{x_4\pi}{180}\right)\frac{\pi}{180}\left(-\frac{1}{a_{12}}x_4\right),$$

$$\psi_{21} = 0, \tag{14e}$$

$$\psi_{22} = -x_3 a_{11} 2 \sin\left(\frac{x_4\pi}{180}\right)\cos\left(\frac{x_4\pi}{180}\right)\frac{\pi}{180}\frac{1}{a_{12}}. \tag{14f}$$

Remark 1. When the load current experiences a step change, the first derivative of the current produces a large peak. In this paper, a first-order filter is used to smooth this peak under the assumption that the current load change rate is finite, as described in detail in [15].

Using the terms d_1 and d_2 to represent the disturbances and unmodeled dynamics, Eq. (13) can be rewritten as

$$\ddot{y}_1 = F_1\left(x, \dot{x}, \xi, \dot{\xi}\right) + \left[\psi_{11}(x) \quad \psi_{12}(x)\right]\left[u_1 \quad u_2\right]^T + d_1, \tag{15a}$$

$$\ddot{y}_2 = F_2\left(x, \dot{x}, \xi, \dot{\xi}\right) + \left[\psi_{21}(x) \quad \psi_{22}(x)\right]\left[u_1 \quad u_2\right]^T + d_2. \tag{15b}$$

Let $z_{1,i} = y_i, z_{2,i} = \dot{y}_i, i \in \{1, 2\}$, and $z_{3,i} = d_i$ represent the extended state. Assuming that d_i is differentiable, we define

$$\dot{d}_i = \phi_i. \tag{16}$$

In this case, Eq. (15) can be rewritten in the following state-space form:

$$\begin{aligned} \dot{z}_{1,i} &= \dot{z}_{2,i} \\ \dot{z}_{2,i} &= F_i\left(x, \dot{x}, \xi, \dot{\xi}\right) + \dot{z}_{3,i} + \left[\psi_{i1} \quad \psi_{i2}\right]\left[u_1 \quad u_2\right]^T, \\ \dot{z}_{3,i} &= \phi_i \\ y_i &= z_{1,i} \end{aligned} \tag{17}$$

and an ESO pertaining to Eq. (17) can be constructed as

$$\begin{aligned} \dot{\hat{z}}_{1,i} &= \hat{z}_{2,i} + 3\omega_{o,i}\left(z_{1,i} - \hat{z}_{1,i}\right) \\ \dot{\hat{z}}_{2,i} &= F_i\left(x, \dot{x}, \xi, \dot{\xi}\right) + \hat{z}_{3,i} + 3\omega_{o,i}^2\left(z_{1,i} - \hat{z}_{1,i}\right) \\ &\quad + \left[\psi_{i1} \quad \psi_{i2}\right]\left[u_1 \quad u_2\right]^T \\ \dot{\hat{z}}_{3,i} &= \omega_{o,i}^3\left(z_{1,i} - \hat{z}_{1,i}\right), \end{aligned} \tag{18}$$

where $\omega_{o,i}$ are positive real numbers representing the observer bandwidth. By denoting $\tilde{z}_{j,i} := z_{j,i} - \hat{z}_{j,i}, j \in \{1, 2, 3\}$, the observation tracking error dynamics can be expressed as [28–30]

$$\begin{aligned} \dot{\tilde{z}}_{1,i} &= \tilde{z}_{2,i} - 3\omega_{o,i}\tilde{z}_{1,i} \\ \dot{\tilde{z}}_{2,i} &= \tilde{z}_{3,i} - 3\omega_{o,i}^2\tilde{z}_{1,i}. \\ \dot{\tilde{z}}_{3,i} &= \phi_i - \omega_{o,i}^3\tilde{z}_{1,i} \end{aligned} \tag{19}$$

Lemma 1. *Assuming that ϕ_i is bounded, there exist a constant $\sigma > 0$ and a finite time $T_1 > 0$ such that $\|\tilde{z}_{j,i}\| \leq \sigma, \forall t \geq T_1 > 0$, and $\omega_{o,i} > 0$. σ is dependent on the initial condition of $\tilde{z}_{j,i}$ and upper boundary of ϕ_i. Furthermore, $\sigma = O(1/\omega_{o,i}^\kappa)$ for $\kappa \in \{1, 2, 3\}$.*

Under the assumption of the boundedness of ϕ_i, Eq. (19) exhibits bounded-input bounded-output stability [30]. The observation tracking error is bounded and can be adjusted by tuning the parameter $\omega_{o,i}$. Then, by replacing the true value $d_i \triangleq z_{3,i}$ with the estimated value $\hat{z}_{3,i}$ of the disturbance (the effect of the deviation between the estimated and true values on the closed-loop stability will be analyzed in detail in the section of "Robustness and performance analysis"), Eq. (15) can be rewritten as follows:

$$\ddot{y}_1 = F_1\left(x, \dot{x}, \xi, \dot{\xi}\right) + \left[\psi_{11}(x) \quad \psi_{12}(x)\right]\left[u_1 \quad u_2\right]^T + \hat{z}_{3,1}, \tag{20a}$$

$$\ddot{y}_2 = F_2\left(x, \dot{x}, \xi, \dot{\xi}\right) + \left[\psi_{21}(x) \quad \psi_{22}(x)\right]\left[u_1 \quad u_2\right]^T + \hat{z}_{3,2}. \tag{20b}$$

3.2. Control law design

Based on Eq. (20), the control inputs u_1 and u_2 are defined as

$$\begin{bmatrix} u_1 \\ u_2 \end{bmatrix} = \begin{bmatrix} \psi_{11} & \psi_{12} \\ \psi_{21} & \psi_{22} \end{bmatrix}^{-1}\begin{bmatrix} \upsilon_1 - F_2\left(x, \dot{x}, \xi, \dot{\xi}\right) - \hat{z}_{3,1} \\ \upsilon_2 - F_2\left(x, \dot{x}, \xi, \dot{\xi}\right) - \hat{z}_{3,2} \end{bmatrix}, \tag{21}$$

where υ_1 and υ_2 are auxiliary variables that will be defined subsequently.

Remark 2. Since all parameters a_ι, $\iota \in \{1, \ldots, 12\}$, are not equal to zero and the flow rate $h(x_1, x_2)$ is monotonically associated with the compressor angular speed x_1, $\frac{\partial h(x_1, x_2)}{\partial x_1} \neq 0$, and $\psi_{11} \neq 0$. In addition, the actual throttle opening angle x_4 cannot be zero or ninety degrees due to its inherent mechanical structure, which means that $\psi_{22} \neq 0$ and $\psi_{21} \equiv 0$. Thus, the matrix $\begin{bmatrix} \psi_{11} & \psi_{12} \\ \psi_{21} & \psi_{22} \end{bmatrix}$ is invertible.

By substituting equation (21) into Eq. (20), the following equation is obtained:

$$\begin{bmatrix} \ddot{y}_1 \\ \ddot{y}_2 \end{bmatrix} = \begin{bmatrix} \upsilon_1 \\ \upsilon_2 \end{bmatrix}, \tag{22}$$

where the control output y_1 is obtained by integrating the auxiliary variable υ_1 twice, and similarly, the control output y_2 but with υ_2. Therefore, υ_1 and υ_2 can be constructed separately to control y_1 and y_2 separately, thereby realizing decoupling. The following expressions are designed:

$$\begin{bmatrix} \upsilon_1 \\ \upsilon_2 \end{bmatrix} = \begin{bmatrix} \ddot{y}_1^* + k_{p1}\left(y_1^* - y_1\right) + k_{d1}\left(\dot{y}_1^* - \dot{y}_1\right) + k_{I1}\int\left(y_1^* - y_1\right) \\ \ddot{y}_2^* + k_{p2}\left(y_2^* - y_2\right) + k_{d2}\left(\dot{y}_2^* - \dot{y}_2\right) + k_{I2}\int\left(y_2^* - y_2\right) \end{bmatrix}, \tag{23}$$

where all the feedback gains are selected as follows:

$$k_{I_1} = \omega_{c_1}^3 \quad k_{P_1} = 3\omega_{c_1}^2 \quad k_{d_1} = 3\omega_{c_1}, \tag{24a}$$

$$k_{I_2} = \omega_{c_2}^3 \quad k_{P_2} = 3\omega_{c_2}^2 \quad k_{d_2} = 3\omega_{c_2}, \tag{24b}$$

where ω_{c_1} and ω_{c_2}, are positive real numbers, determining the closed-loop pole positions. By substituting equation (23) into Eq. (21), the final feedback control law can be obtained:

$$\begin{bmatrix} u_1 \\ u_2 \end{bmatrix} = \begin{bmatrix} \psi_{11} & \psi_{12} \\ \psi_{21} & \psi_{22} \end{bmatrix}^{-1} \begin{bmatrix} \ddot{y}_1^* + k_{p1}\left(y_1^* - y_1\right) + k_{d1}\left(\dot{y}_1^* - \dot{y}_1\right) + k_{I1}\int\left(y_1^* - y_1\right) \\ -F_1\left(x, \dot{x}, \xi, \dot{\xi}\right) - \hat{z}_{3,1} \\ \ddot{y}_2^* + k_{p2}\left(y_2^* - y_2\right) + k_{d1}\left(\dot{y}_2^* - \dot{y}_2\right) + k_{I2}\int\left(y_2^* - y_2\right) \\ -F_2\left(x, \dot{x}, \xi, \dot{\xi}\right) - \hat{z}_{3,2} \end{bmatrix}. \tag{25}$$

3.3. Robustness and performance analysis

Substituting equation (25) into Eq. (15) yields

$$\begin{bmatrix} \ddot{y}_1 \\ \ddot{y}_2 \end{bmatrix} = \begin{bmatrix} \ddot{y}_1^* + k_{p1}\left(y_1^* - y_1\right) + k_{d1}\left(\dot{y}_1^* - \dot{y}_1\right) \\ +k_{I1}\int\left(y_1^* - y_1\right) + \tilde{z}_{3,1} \\ \ddot{y}_2^* + k_{p2}\left(y_2^* - y_2\right) + k_{d2}\left(\dot{y}_2^* - \dot{y}_2\right) \\ +k_{I2}\int\left(y_2^* - y_2\right) + \tilde{z}_{3,2} \end{bmatrix}. \tag{26}$$

By defining $e_i = (y_i^* - y_i)$, $i \in \{1, 2\}$, Eq. (26) can be rewritten as

$$\begin{bmatrix} \ddot{e}_1 + k_{d1}\dot{e}_1 + k_{p1}e_1 + k_{I1}\int e_1 \\ \ddot{e}_2 + k_{d2}\dot{e}_2 + k_{p2}e_2 + k_{I2}\int e_2 \end{bmatrix} = \begin{bmatrix} \tilde{z}_{3,1} \\ \tilde{z}_{3,2} \end{bmatrix}. \tag{27}$$

According to the Laplace transform, Eq. (27) can be rewritten as

$$E_1(S) = \frac{1}{S^2 + k_{d1}S + k_{p1} + \frac{k_{I1}}{S}}\tilde{z}_{3,1}(S)$$
$$E_2(S) = \frac{1}{S^2 + k_{d2}S + k_{p2} + \frac{k_{I2}}{S}}\tilde{z}_{3,2}(S). \tag{28}$$

According to the classical control theory, the closed-loop transfer function of the tracking error (28) is stable as long as all the poles are negative. Because the disturbance is mainly caused by the temperature and humidity with slow varying characteristics (introduced in the section of "Model validation") and the item $\tilde{z}_{3,i}$ is bounded according to Lemma 1, the term $\tilde{z}_{3,i}$ can be
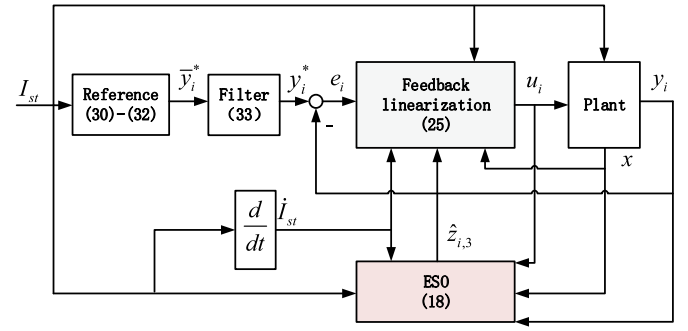

Fig. 7. Structure of the suggested control strategy for an air supply subsystem.

approximated as a step signal of amplitude $A_i(\tilde{z}_{3,i})$. The final value theorem provides a representation of the steady-state error

$$e_{1,\infty} = \lim_{S \to 0} S\frac{A_1(\tilde{z}_{3,1})}{S}\frac{S}{S^3 + k_{d1}S^2 + k_{p1}S + k_{I1}} = 0$$
$$e_{2,\infty} = \lim_{S \to 0} S\frac{A_2(\tilde{z}_{3,2})}{S}\frac{S}{S^3 + k_{d2}S^2 + k_{p2}S + k_{I2}} = 0. \tag{29}$$

3.4. Controller implementation

The reference air flow rate W_{sm}^* can be expressed as a function related to the load current and optimal oxygen excess ratio $\lambda_{O_2}^*$ as

$$W_{sm}^* = \frac{1}{x_{o_2}}\frac{n_{cell}I_{st}}{4F}\lambda_{O_2}^*, \tag{30}$$

where $x_{o_2} = 0.21$ represents the oxygen mass fraction in air and $\lambda_{O_2}^*$ can be expressed as [31]

$$\lambda_{O_2}^* = 5 \times 10^{-8}I_{st}^3 - 2.87 \times 10^{-5}I_{st}^2 + 2.23 \times 10^{-3}I_{st} + 2.5. \tag{31}$$

In addition, the reference cathode pressure p_{ca}^* usually follows the anode pressure and is positively related to the load current [5]:

$$p_{ca}^* = 0.01542 \times I_{st}^3 - 10.25 \times I_{st}^2 + 2327 \times I_{st} - 28240. \tag{32}$$

To obtain smooth $\dot{y}_i^*$ and $\ddot{y}_i^*$, $i \in \{1, 2\}$, two second-order low-pass filters are used to process the signal. The original reference signal $\bar{y}_i^*$ passes through the filters to yield

$$\frac{y_i^*}{\bar{y}_i^*} = \frac{\omega_{n,i}^2}{s^2 + 2\zeta_i\omega_{n,i}s + \omega_{n,i}^2}. \tag{33}$$

The overall structural diagram is shown in Fig. 7. First, according to the load current, the smooth outputs y_i^* and their first and second derivatives are obtained using the second-order filter. The tracking error and disturbances as well as the plant's nonlinear part act on the feedback linearization to obtain the final control law.

4. Simulation results

The effectiveness of the proposed nonlinear multivariable control is investigated by a series of simulations.

The first series of simulations are conducted to verify the estimation and compensation performance of the ESO in the case of unknown disturbances, including model mismatch and uncertainties in the environmental parameters. The current load, throttle opening angle command and compressor voltage are shown in Fig. 5. Fig. 8 shows the comparison curves of the air flow rate into the cathode and cathode pressure between the plant and model with the ESO. The maximum flow rate error is 0.00038 kg/s, and the relative error is 0.5% at 14.5 s. The
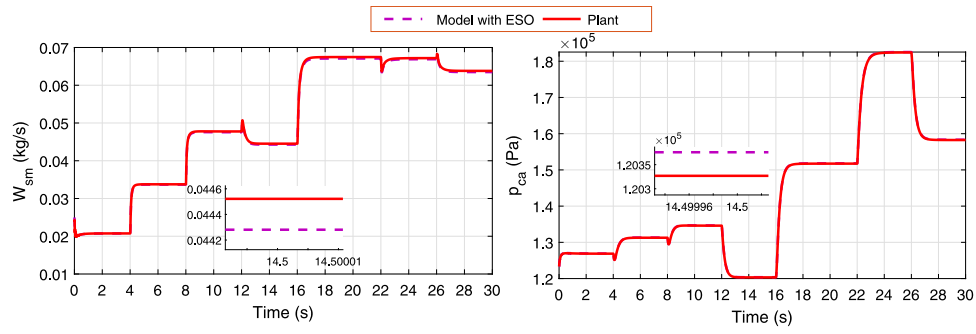
Fig. 8. Comparison between the plant and model with the ESO.
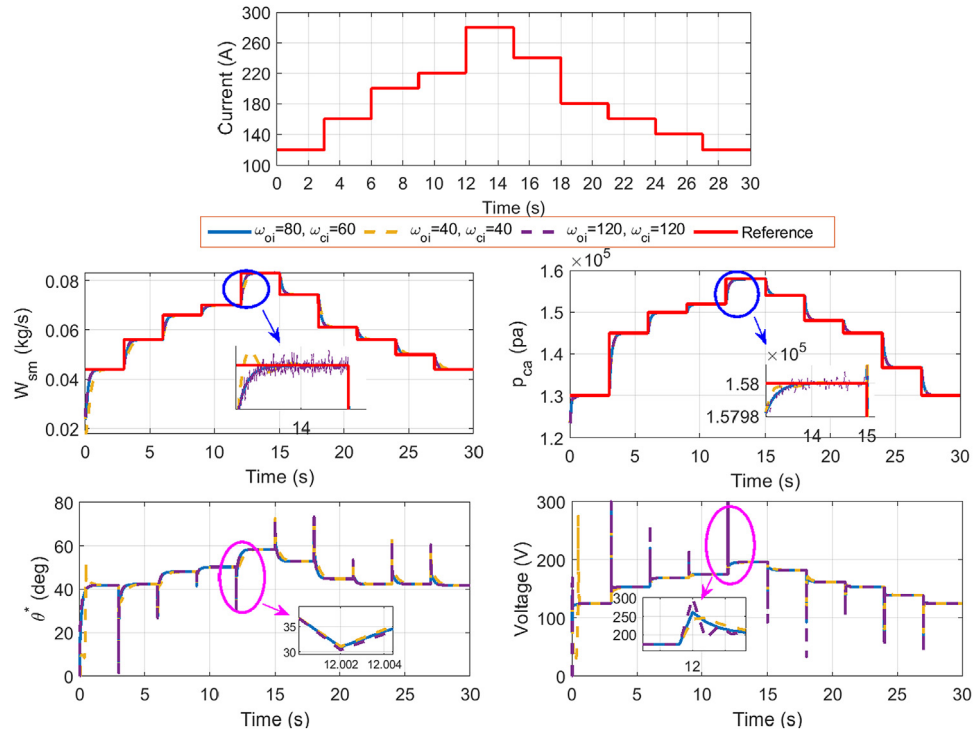

Fig. 9. Simulation results under different gains of the ESO and control law. (For interpretation of the references to color in this figure legend, the reader is referred to the web version of this article.)
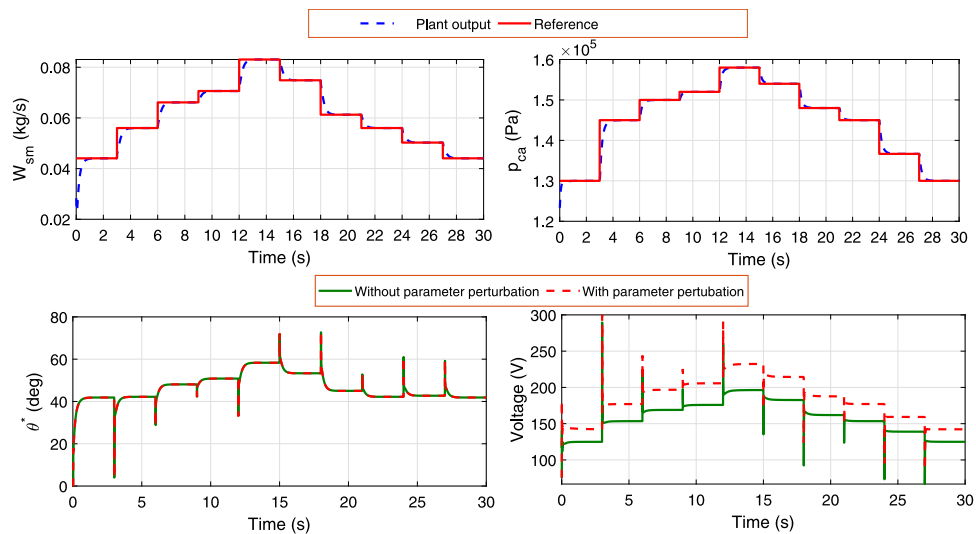

Fig. 10. Simulation results: testing involving perturbed model parameters.
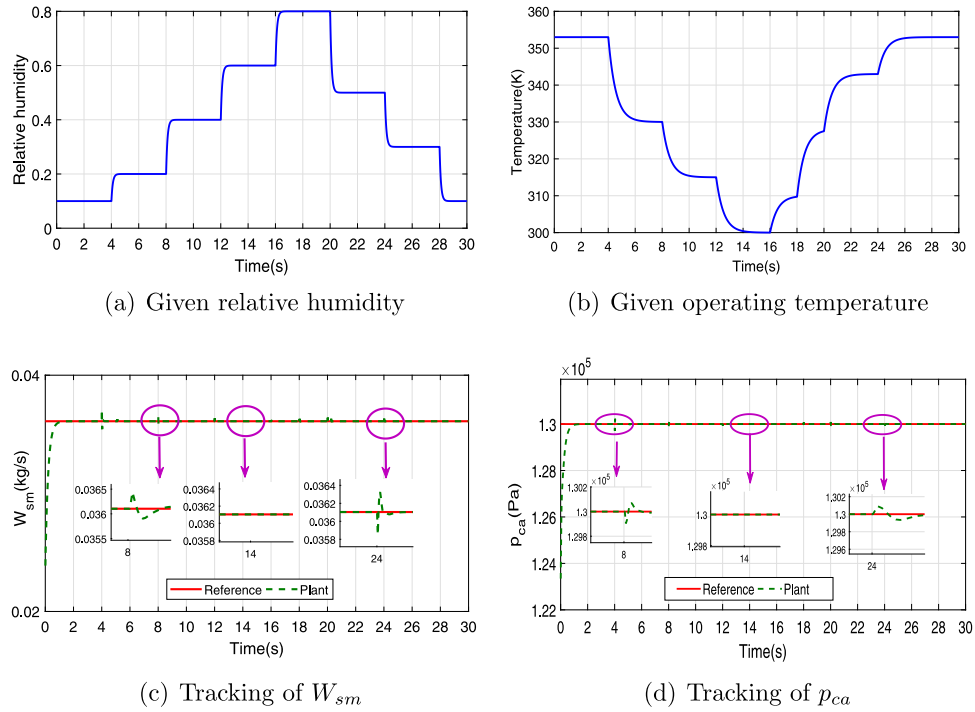
(a) Given relative humidity

(b) Given operating temperature

(c) Tracking of W_{sm}

(d) Tracking of p_{ca}

Fig. 11. Simulation results: testing with external environment disturbances.
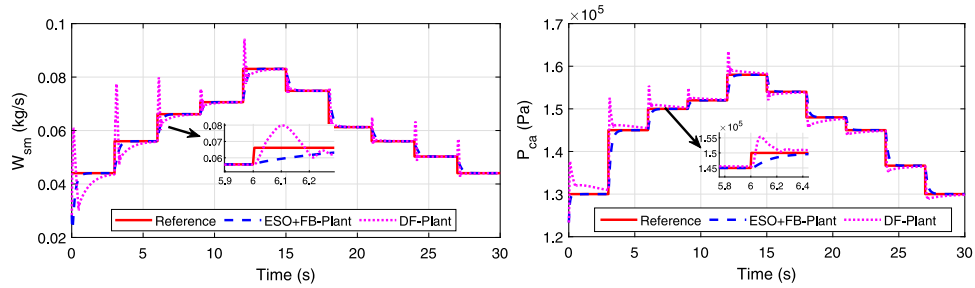

Fig. 12. Simulation results: comparison between ESO+FB and DF when the reference input is not filtered in the DF method.
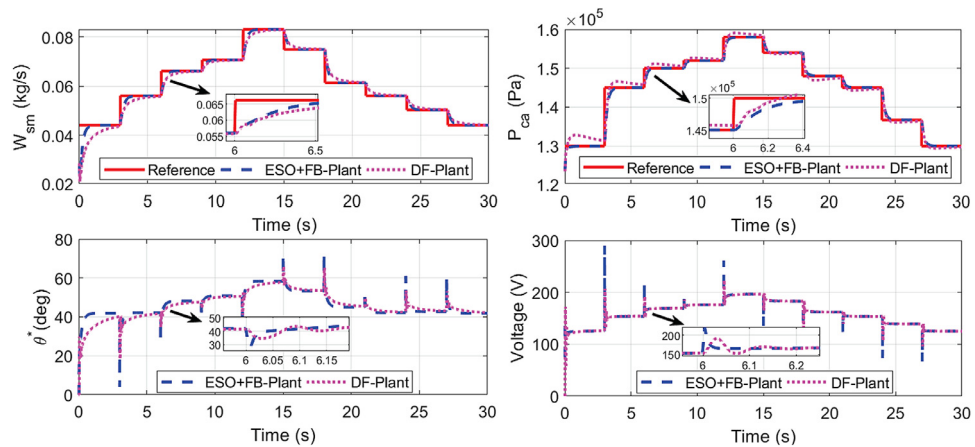

Fig. 13. Simulation results: comparison between ESO+FB and DF when the reference input is filtered in the DF method.

maximum cathode pressure error is 100 Pa, and the relative error is 0.066% at 14.5 s. The simulation results indicate that the model with the ESO can reflect the dynamic characteristics of plants with high precision and overcome the adverse influences of the disturbances.

This work analyzes the impact of the gains of the ESO and the control law on the outputs in the second series of simulations. As can be seen from Fig. 9, a series of continuously increasing load current sequences from 120 A to 280 A is employed, followed by a steep decline from 280 A to 120 A. Control outputs and control

Table 3
Range of parameter perturbations.

Motor constant: k_t	+5%	Compressor inertia: J_{cp}	−10%
Motor constant: k_v	+5%	Volume of air supply manifold: V_{sm}	+10%
Compressor resistance: R_{cm}	+10%	Volume of cathode: V_{ca}	−10%

inputs with large feedback gains are more sensitive to tracking deviations, resulting in significant chattering (Purple dotted line: $\omega_{o_i} = 120$, and $\omega_{c_i} = 120$). Conversely, outputs and inputs with small gains have a slow dynamic response (Yellow dashed line: $\omega_{o_i} = 40$, and $\omega_{c_i} = 40$). In order to trade off the response rapidity and the smoothness of outputs and inputs, the gains are selected as follows (Blue solid line: $\omega_{o_i} = 80$, and $\omega_{c_i} = 60$).

The third series of simulations are conducted under the condition of model parameter perturbation to demonstrate the controller's performance in suppressing changes in the model parameters. The range of parameter perturbations is given in Table 3. As illustrated in Fig. 10, the simulation results correspond to a satisfactory tracking performance, which indicates that the proposed control strategy can smoothly and stably track the reference when the parameters are perturbed. The profiles of the manipulated variables with and without parametric perturbations show that the steady-state value of the compressor supply voltage deviates, while the throttle opening command does not change significantly. This phenomenon occurs because the parameter perturbations, set in Table 3, are derived from the compressor and not the throttle. The throttle model considered in this paper has a closed-loop control structure (the throttle model is approximately a first-order system obtained through inner closed-loop control), and thus, its parameter perturbations are suppressed in the inner closed loop.

To further explore the robustness of the controller against external environment disturbances, a fourth series of simulations are conducted in which the relative humidity is randomly set to vary from 10% to 80% to 10% and the working temperature varies from 353.15 K to 300 K to 353.15 K inside the PEMFC. The corresponding profiles are shown in Figs. 11(a) and 11(b). The response results of the control outputs are shown in Figs. 11(c) and 11(d). From the simulation results for 14 s in Fig. 11(c), the air flow rate follows the optimal reference value without steady-state error when the working temperature and relative humidity are constant. When the environmental parameters rise or fall steeply, the flow rate vibrates with a small amplitude and promptly returns to the steady value, as indicated by the simulation results for 8 s and 24 s. The maximum amplitude of deviation from the steady-state value is less than 0.001 kg/s, the relative error is 2.85%, and the time to return to the steady-state value is less than 0.06 s. Similarly, as shown in the simulation results for 14 s in Fig. 11(d), the cathode pressure tracking curve is smooth for specific environmental parameters. The simulation results at 8 and 24 s show the cathode pressure tracking process when the environmental parameters change. The maximum amplitude of deviation from the steady state is less than 200 Pa, the relative error is 0.154%, and the dynamic process ends within 0.18 s. Hence, the controller exhibits a good rejection performance against external disturbances.

Finally, we compare the proposed control strategy (ESO+FB) with the differential flatness (DF) method reported in [24] to illustrate the superiority of the ESO+FB approach. Fig. 12 shows the profile of the control outputs when the reference input is not filtered in the DF method. The tracking curve of DF is highly intense, accompanied by an overshoot, and takes longer to return to the steady-state value when a step change occurs in the reference input. Fig. 13 shows the profile of the control outputs when the reference input is filtered in the DF method. For DF, the time to return to the steady state is longer than that for ESO+FB, and the

Table A.1
Physical parameters.

Symbol	Description	Value [Unit]
J_{cp}	Compressor inertia	$5*10^{-5}$ [kg m^2]
R_{cm}	Compressor resistance	0.9 [Ω]
η_{cm}	Mechanical efficiency	90 [%]
k_t	Motor constant	0.0153 [V/(rad/s)]
k_v	Motor constant	0.0153 [N-m/A]
C_p	Specific heat capacity	1004 [J kg^{-1} K^{-1}]
T_{atm}	Atmosphere temperature	298.15 [K]
η_{cp}	Maximum efficiency of the compressor	80 [%]
γ	Ratio of specific heat	1.4 [–]
p_{atm}	Atmospheric pressure	101 315 [pa]
R_a	Air gas constant	298.6 [J/(kg K)]
V_{sm}	Volume of the air supply manifold	0.02 [m^3]
k_{sm}	Flow constant	$0.3629*10^{-5}$ [kg/(s Pa)]
R_{O_2}	Oxygen gas constant	259.8 [J/(kg K)]
M_{O_2}	Oxygen molar mass	0.032 [kg/mol]
V_{ca}	Volume of the cathode	0.01 [m^3]
T_{st}	Temperature of the cathode	353.15 [K]
n_{cell}	Number of cells	381 [–]
F	Faraday number	96 485 [–]
$C_{D,tr}$	Throttle discharge coefficient	0.0248 [–]
$A_{T,tr}$	Maximum throttle opening area	0.002 [m^2]
$\bar{R}$	Universal gas constant	8.3145 [J/(mol K)]
T_{tr}	Response time constant of the throttle	0.04 [–]

tracking curve is not smooth, exhibiting jitter. In contrast, ESO+FB exhibits not only a fast dynamic response but also a smooth curve without any overshoot. These results show that the proposed ESO+FB strategy can provide superior dynamic and steady-state characteristics for synergistic control of the air supply subsystem.

5. Conclusion

To simultaneously regulate the air flow rate into the cathode and cathode pressure in the air supply subsystem, a disturbance-observer-based feedback linearization control strategy is developed. This control technique is based on a simplified model derived from a complete nonlinear model of the air supply subsystem, in which, experimental data of the compressor are obtained through multiple sets of tests. Since the simplified model is used for the controller design, an extended state observer is implemented to observe the disturbances and unmodeled dynamics. The simulation results verify that the simplified model with disturbance observation exhibits close dynamic characteristics as the plant, with relative errors of 0.5% and 0.066% for the air flow rate and cathode pressure, respectively. The final control law, obtained through the feedback linearization, is employed for the air supply subsystem. A series of simulations are implemented under different operating conditions, exhibiting good results in terms of a dynamic response time of less than 0.9 s, no steady-state tracking error, and strong robustness against disturbances and unmodeled dynamics. A final comparison of the simulation results shows that the control strategy designed in this paper exhibits a smoother dynamic response and requires less time to reach the steady state.

Declaration of competing interest

The authors declare that they have no known competing financial interests or personal relationships that could have appeared to influence the work reported in this paper.

Acknowledgments

Appendix

See Table A.1

References

[1] Ma J, Liu X, Zou X, Yue M, Shang P, Kang L, Jemei S, Lu C, Ding Y, Zerhouni N, et al. Degradation prognosis for proton exchange membrane fuel cell based on hybrid transfer learning and intercell differences. ISA Trans 2020;113:149–65.

[2] Wang Y, Chen KS, Mishler J, Cho SC, Adroher XC. A review of polymer electrolyte membrane fuel cells: Technology, applications, and needs on fundamental research. Appl Energy 2011;88(4):981–1007.

[3] Zhang D, Baraldi P, Cadet C, Yousfi-Steiner N, Bérenguer C, Zio E. An ensemble of models for integrating dependent sources of information for the prognosis of the remaining useful life of Proton Exchange Membrane Fuel Cells. Mech Syst Signal Process 2019;124:479–501.

[4] Wang GL, Wang Y, Shi JH, Shao HH. Coordinating IMC-PID and adaptive SMC controllers for a PEMFC. ISA Trans 2010;49(1):87–94.

[5] Al-Durra A, Yurkovich S, Guezennec Y. Study of nonlinear control schemes for an automotive traction PEM fuel cell system. Int J Hydrogen Energy 2010;35(20):11291–307.

[6] Han J, Yu S, Yi S. Adaptive control for robust air flow management in an automotive fuel cell system. Appl Energy 2017;190(15):73–83.

[7] Danzer MA, Wilhelm J, Aschemann H, Hofer EP. Model-based control of cathode pressure and oxygen excess ratio of a PEM fuel cell system. J Power Sources 2008;176(2):515–22.

[8] Ramos-Paja CA, Giral R, Martinez-Salamero L, Romano J, Romero A, Spagnuolo G. A PEM fuel-cell model featuring oxygen-excess-ratio estimation and power-electronics interaction. IEEE Trans Ind Electron 2009;57(6):1914–24.

[9] Na W, Gou B. Feedback-linearization-based nonlinear control for PEM fuel cells. IEEE Trans Energy Convers 2008;23(1):179–90.

[10] Hillstrom E, Canova M, Guezennec Y, Rizzoni G. Modeling the cathode pressure dynamics in the Buckeye Bullet II 540 kW hydrogen PEM fuel cell system. J Power Sources 2013;241:33–45.

[11] Pukrushpan JT. Modeling and control of fuel cell systems and fuel processors. University of Michigan; 2003.

[12] Suh KW. Modeling, analysis and control of fuel cell hybrid power systems. University of Michigan; 2006.

[13] Talj RJ, Hissel D, Ortega R, Becherif M, Hilairet M. Experimental validation of a PEM fuel-cell reduced-order model and a moto-compressor higher order sliding-mode control. IEEE Trans Ind Electron 2009;57(6):1906–13.

[14] Ramospaja CA, Giral R, Martinezsalamero L, Romano J, Romero A, Spagnuolo G. Simplified mathematical model of proton exchange membrane fuel cell based on horizon fuel cell stack. Mod Power Syst 2016;4(4):668–79.

[15] Chen J, Liu Z, Wang F, Ouyang Q, Su H. Optimal oxygen excess ratio control for PEM fuel cells. IEEE Trans Control Syst Technol 2017;26(5):1711–21.

[16] Kunusch C, Puleston PF, Mayosky MA, Riera J. Sliding mode strategy for PEM fuel cells stacks breathing control using a super-twisting algorithm. IEEE Trans Control Syst Technol 2008;17(1):167–74.

[17] Liu J, Gao Y, Su X, Wack M, Wu L. Disturbance-observer-based control for air management of PEM fuel cell systems via sliding mode technique. IEEE Trans Control Syst Technol 2018;27(3):1129–38.

[18] Pilloni A, Pisano A, Usai E. Observer-based air excess ratio control of a PEM fuel cell system via high-order sliding mode. IEEE Trans Ind Electron 2015;62(8):5236–46.

[19] Garcia-Gabin W, Dorado F, Bordons C. Real-time implementation of a sliding mode controller for air supply on a PEM fuel cell. J Process Control 2010;20(3):325–36.

[20] Ma Y, Zhang F, Gao J, Chen H, Shen T. Oxygen excess ratio control of PEM fuel cells using observer-based nonlinear triple-step controller. Int J Hydrogen Energy 2020;45(54):29705–17.

[21] Hu Y, Chen H, Gong X, Yu S, Gao J, Chen H. Control-oriented modeling and robust nonlinear triple-step controller design for an air-feed system for polymer electrolyte membrane fuel cells. Asian J Control 2019;21(4):1811–23.

[22] Gruber J, Bordons C, Oliva A. Nonlinear MPC for the airflow in a PEM fuel cell using a Volterra series model. Control Eng Pract 2012;20(2):205–17.

[23] Ouyang Q, Chen J, Wang F, Su H. Nonlinear MPC controller design for AIR supply of PEM fuel cell based power systems. Asian J Control 2017;19(3):929–40.

[24] Da Fonseca R, Bideaux E, Gerard M, Jeanneret B, Desbois-Renaudin M, Sari A. Control of PEMFC system air group using differential flatness approach: validation by a dynamic fuel cell system model. Appl Energy 2014;113(1):219–29.

[25] Gao J, Li M, Hu Y, Chen H, Ma Y. Challenges and developments of automotive fuel cell hybrid power system and control. Sci China Inf Sci 2019;62(2):50–74.

[26] Gravdahl JT, Egeland O. Compressor surge & rotating stall. Springer; 2012.

[27] Heywood JB. Internal combustion engine fundamentals. McGraw-Hill Education; 2018.

[28] Han J. From PID to active disturbance rejection control. IEEE Trans Ind Electron 2009;56(3):900–6.

[29] Talole SE, Kolhe JP, Phadke SB. Extended-state-observer-based control of flexible-joint system with experimental validation. IEEE Trans Ind Electron 2009;57(4):1411–9.

[30] Zheng Q, Chen Z, Gao Z. A practical approach to disturbance decoupling control. Control Eng Pract 2009;17(9):1016–25.

[31] Zhang H, Wang Y, Wang D, Wang Y. Adaptive robust control of oxygen excess ratio for PEMFC system based on type-2 fuzzy logic system. Inform Sci 2017;511:1–17.